Numerical Analysis of Heterogeneous Engineering Materials

Lesičar, T., Sorić, J., Tonković, Z.

Faculty of Mechanical Engineering and Naval Architecture
tomislav.lesicar@fsb.hr, jurica.soric@fsb.hr, zdenko.tonkovic@fsb.hr

Abstract: A heterogeneous material such as nodular cast iron is widely used as a material of engineering structural components. The realistic description of its deformation responses demands an accurate modelling at both macroscopic and microscopic scales. In this paper a two-scale computational approach employing the homogenization scheme based on the small strain nonlocal continuum theory is presented. Discretization at both scales is performed by means of the C^1 continuity finite element developed by using the strain gradient theory. After the scale transition procedure and the homogenization approach at the microlevel, the constitutive relations are computed at each material point at the macroscale predicting the structural deformation response. All algorithms derived were embedded into the finite element program ABAQUS. The performance and accuracy of the proposed approach was verified in an example, where the microstructure of a nodular cast iron is modelled by an academic representative volume element.

Keywords: heterogeneous materials, second-order homogenization, C^1 finite element, nonlocal continuum theory

1. Introduction

Many engineering materials have a heterogeneous structure, and they are often referred to as multi-phase materials, composite or heterogeneous materials. From an engineering point of view, multi-phase materials are desirable because they can be tailor-made to take advantage of particular properties of each constituent. Besides rock, concrete, wood, fibre-reinforced composites and other similar materials, metals such as nodular cast iron are widely used as a material for structural components in mechanical engineering. The nodular cast iron consists of graphite spheroids or nodules, positioned in an either ferritic or pearlitic matrix, providing large

fatigue strength. The size, shape, spatial distribution, volume fraction and the properties of the constituents making up the microstructure have a significant impact on the behaviour of material properties observed at the macroscale.

Modelling of the mechanical behaviour of heterogeneous materials represents an essential issue in engineering. In recent years the investigation of the relations between mechanical properties of material and its microstructure became very attractive topic, considering that almost all materials are heterogeneous at lower scales. Depending on the material microstructure, size effects can be observed, resulting in different mechanical behaviours (Fleck and Hutchinson, 1993, 2001). Unfortunately, the classical continuum theory cannot capture such effects, since it does not contain an internal length scale. As a remedy, extension towards the higher-order continuum theory has been proposed. The first significant work in extension to the higher-order continuum theory originates from Cosserat brothers (Cosserat and Cosserat, 1909), which gave a first systematic review of a three-dimensional solid. Unfortunately, the potential of this generalization was not recognized until the early sixties of the last century. Important developments in higher-order theories were achieved during the 1960's (Mindlin and Tiersten, 1962; Koiter, 1963; Toupin, 1964). Pioneering achievements in this full second-gradient theory were established in (Mindlin, 1965) with introduction of the double stress tensor as the work conjugate to second derivative of the displacement field. Also, there are approaches introducing a material with the microstructure (Germain, 1973), where each point has its own degrees of freedom. In the last few decades advantages of the higher- order theories have been recognized as a valuable tool for modelling of material elastoplasticity derived within the gradient dependent plasticity as well as for the damage modelling (de Borst, Pamin and Geers, 1999; Putar *et al.*, 2017). Due to higher-order gradients available, the description of the localization phenomena and material softening is possible without loss of ellipticity of governing equations. Furthermore, with introduction of an intrinsic length scale, the size effects, which can be very often observed in experimental investigations, can be efficiently described by means of numerical algorithms. For more details on the review of gradient continua, see (Zhu, Zbib and Aifantis, 1997; Maugin and Metrikine, 2010).

For the solution of practical problems analytical solutions for the higher-order continua may be obtained only for a few very simple problems. Consequently, finding solution to the problem using the numerical analysis, for example, the finite element method is necessary. The higher- order displacement gradients invoked in the virtual work statement lead to a higher-order differential equation. Numerical solution of this governing equation requires a higher interpolation scheme, where C^1 continuity must be ensured. In the finite element framework this brings necessity for a higher-order finite element formulation supporting additional degrees of freedom (Argyris, Fried and Scharpf, 1968). On the other hand, structural complexity of the element also increases (Clough and Tocher, 1965). Increased complexity of

the finite element formulation as well as inconvenient numerical implementation are the main reasons that these elements are not too attractive for practical use. Therefore, many efforts have been undertaken trying to simulate gradient problems compensating requirement for C^1 interpolations. In this field many methods have been developed, for example, the implicit methods (Askes, Bennett and Aifantis, 2007), the mixed formulations where kinematic relation between displacements and displacement derivatives is enforced by Lagrange multipliers (Amanatidou and Aravas, 2002), or by penalty functions (Zervos, Papanicolopulos and Vardoulakis, 2009) and the micromorphic continuum formulations with Lagrange multipliers (Shu, King and Fleck, 1999) or penalty parameters (Britta Hirschberger, Kuhl and Steinmann, 2007). Unfortunately, alternative approaches suffer from drawbacks, resulting in locking and unphysical results. A comprehensive state-of-the-art of C^1 continuous finite element formulations is given in (Fischer, Steinmann and Willner, 2011).

To accurately predict the mechanical response of the evolving microstructure, the multiscale approach is required, integrating physical understanding of material behaviour at various physical scales. A rapid increase in computational power boosted by innovative solutions in numerical modelling has enabled detailed quantification of the mechanical response of materials across multiple scales for nonlinear processes. Using the multiscale setting we are able to develop constitutive models applicable at engineering scales using detailed information obtained from finer scales through application of newly developed class of computational homogenization methods.

The overall concept of the computational homogenization was developed in (Suquet, 1985) and its main attention is determination of the effective properties of heterogeneous media. The computational homogenization allows the incorporation of the microstructure into a standard continuum model turning standard boundary value problem into a nested boundary value problem, containing the macroscale and the microscale level. In such a scheme an explicit macroscopic material model is not available. Instead, it is provided by the locally attached microscopic boundary value problem driven by macroscopic quantities. However, a finer scale geometry (microstructure) is often unknown, so statistical assumptions have to be made. Macroscopic properties are determined by the homogenization process acting on the effective, homogenized sample of material called statistically Representative Volume Element (RVE), see for example (Stroeven, Askes and Sluys, 2004; Gitman, Gitman and Askes, 2006). The resulting effective material is supposed to represent all macroscopic properties of the microheterogeneous structure and enables to restrict the computational effort to the smallest, still representative, material sample. Firstly developed concepts of computational homogenization techniques are built within the standard local continuum mechanics, where the behaviour of the material point depends only on the first gradient of the displacement field, re-

ferred to as the first-order homogenization. Unfortunately, the first-order micro-macro computational approaches, as well as the conventional homogenization methods, have some major disadvantages. As first, even though the first-order homogenization technique accounts for an influence of the heterogeneous microstructure by explicit modelling of the microconstituents, it cannot take into account the absolute size of the microstructure. Consequently, geometrical size effects cannot be accounted for. On the other hand, from the mathematical point of view the first-order approach relies on the intrinsic assumption of uniformity of the macroscopic stress and strain fields appointed to RVE. Due to uniformity assumption the first-order homogenization is not appropriate for problems dealing with high gradients, where the macroscopic fields can vary rapidly. To overcome these shortcomings, the second-order computational homogenization procedure, as extension of the classical computational homogenization was proposed (Sluis *et al.*, 1999). To derive the second-order homogenization, the nonlocal continuum theory satisfying C^1 continuity has to be used at the macroscale. In this way the first and the second gradient of the displacement field at the macrolevel are prescribed through the essential boundary conditions on the RVE. At the microscale, RVE is still treated as an ordinary continuum, described by the standard continuum theory using well known constitutive equations. From the solution of the RVE boundary value problem, the stress, double stress tensor and constitutive matrices giving the higher-order continuum constitutive behaviour are extracted from the homogenization procedure. Even though the second-order computational homogenization approach has many advantages, the scale transition of variables between two different continuum approaches suffers from several drawbacks, as revealed in (Luscher, McDowell and Bronkhorst, 2010).

Hence, a new multiscale algorithm based on the nonlocal second-order computational homogenization was presented in this contribution. In comparison to available multiscale approaches employing the second-order computational homogenization, the proposed algorithm preserves the nonlocal theory at both the macrolevel and the microlevel. The modified strain gradient elasticity theory (Ru and Aifantis, 1993), assuming the linear elastic material behaviour and small strain, has been adopted. The discretization at both scales was performed by the C^1 continuity plane strain triangular finite element derived in (Lesičar, Tonković and Sorić, 2014). A consistent nonlocal homogenization scheme was proposed. The derived scale transition methodology, as well as homogenization procedure were embedded into the finite element program ABAQUS by means of FORTRAN subroutines. The performance and accuracy of the proposed approach was verified on an example dealing with the elastic three-point bending test. The microstructural RVE describes a nodular cast iron structure in an academic way.

The paper is organized as follows. In Section 2 the nodular cast iron representing a heterogeneous material is described in more detail. Section 3 deals with the numer-

ical modelling of the heterogeneous material. Therein the basic relation of the non-local continuum and the finite element derivation are presented. In Section 4 the two-scale transition together with the homogenization approach and numerical implementation are described. The numerical example is presented in Section 5. In the last Section 6 concluding remarks are given.

2. Heterogeneous materials in engineering applications

One of highly heterogeneous material which has a wide application in industrial structural components is nodular cast iron. The determination of its mechanical properties was in the focus of a considerable amount of research during the past several decades. This section provides an overview of the authors' studies that are performed in order to investigate the influence of the microstructure on the mechanical behaviour of the nodular cast iron. It is an iron - carbon alloy which has mechanical properties similar to steel. However, in comparison to steel, nodular cast iron reduces production cost and weight of structural components. In addition, it has superior castability and machinability. For these reasons, it is widely used in energy equipment and transportation and nuclear industries, such as wind turbine components, vehicle industry, shipbuilding, pipes or nuclear storage, transportation casks and many other cyclically loaded structures (Minnebo, Nilsson and Blagoeva, 2007; Shirani and Härkegård, 2011; Šamec, Potrč and Šraml, 2011).

Nodular cast iron consists of graphite spheroids or nodules, dispersed in an either ferritic or pearlitic metal matrix. In general, the ductile iron with the ferritic matrix exhibits lower yield and tensile strength, but higher elongation and toughness. The pearlitic matrix has the opposite effect on the mechanical properties. A matrix with both ferritic and pearlitic phases with intermediate mechanical properties is often found in practice. Besides the matrix microstructure, the fatigue strength of nodular cast iron is influenced by the graphite morphology (size, shape and distribution of graphite nodules) (Hübner *et al.*, 2007; Costa, Machado and Silva, 2008, 2010).

The results of experimental studies on the mechanical behaviour of ductile nodular cast iron EN-GJS-400-18-LT depending on the material microstructure are well elaborated in the previous publications of the authors' research team (Čanžar, P., Tonković, Z., Bakić, A., Kodvanj, 2011; Čanžar, Tonković and Kodvanj, 2012; Čanžar, P. and Tonković, 2014). In this section, a short description of the test procedure is given, and some selected test results are presented. The cyclic deformation and fatigue behaviour of four types of cast iron produced by different technologies are considered. The investigated material was provided by the company MIV Varaždin of Croatia. Herein, some results for two types of the cast iron produced

by flotret (Type 200) and inmould (Type 400) techniques are presented. The graphite morphology of the casting types is shown in Fig. 1, while the microstructural data are presented in Table 1. As may be seen, both materials have a predominantly ferritic matrix, where the perlite content is not more than 7%. Furthermore, material type 200 produced by the flotret process has significantly larger nodules with low density distribution than type 400 of nodular cast iron. Besides, the material type 200 has graphite nodules with the lowest circularity (irregularly shaped nodules). On the other hand, material type 400 produced by the inmould process has smaller ferrite grains and smaller nodules, more spherical and regular in shape than those in material type 200.

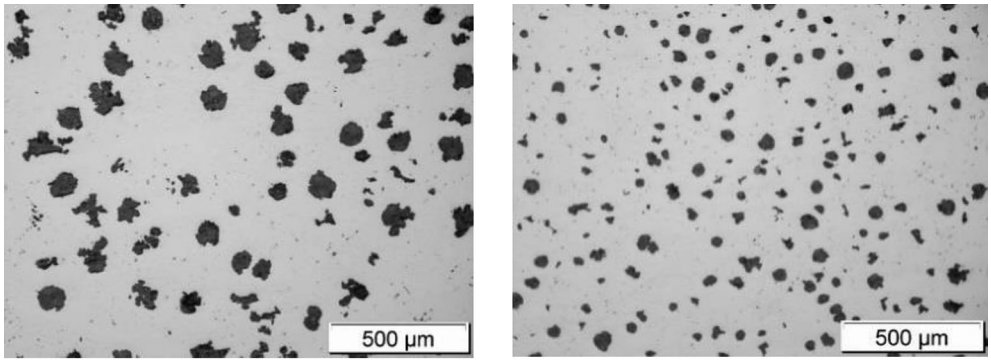

Fig. 1 – The microstructure of nodular cast iron: (a) type 200 and (b) type 400 (Čanžar, 2012; Čanžar, Tonković and Kodvanj, 2012)

Table 1 – Metallographic characteristics of nodular cast iron (Čanžar, 2012; Čanžar, Tonković and Kodvanj, 2012)

Material type	Graphite nodules			Pearlite	
	Number (mm^2)	Average size (µm^2)	Circularity	Area (µm^2)	%
200	57	1,416.80	0.57	49,925.41	4.99
400	81	837.09	0.66	69,726.31	6.97

Monotonic tensile, cyclic and fatigue tests were performed on the servo-hydraulic fatigue testing machines Walter Bai LFV 50-HH, MESSPHYSIK BETA 50-5 and INSTRON 8801 with a load capacity of ±50 kN. Monotonic tensile tests are carried out on flat specimens (Krstulović-Opara *et al.*, 2015). The loading process was acquired by the infrared (IR) thermography and the 3D Digital Image Correlation (DIC). In Fig. 2 the loading sequence images obtained for 10 mm/s loading velocity are presented. The images in Figs. 2(a), obtained by the 3D DIC show the von

Mises equivalent strain distribution. The infrared thermal images in Figs. 2(b) present the thermal distribution proving that generated heat is a consequence of plastic deformation. As presented in (Krstulović-Opara *et al.*, 2015), the generated heat acquired by the IR camera is equivalent to equivalent plastic strain distribution acquired by the 3D DIC (Fig. 2). Therefore, the optical techniques showed to be a powerful tool for the development and calibration of constitutive models from full-field measurements of displacements and strains. The mechanical properties of the nodular cast iron Type 200 obtained from the monotonic tensile test are as follows: yield strength of 256.5 MPa, tensile strength of 417.2 MPa, modulus of 182.4 GPa and elongation of 23.5%, respectively. The nodular cast iron type 400 has very similar monotonic tensile properties.

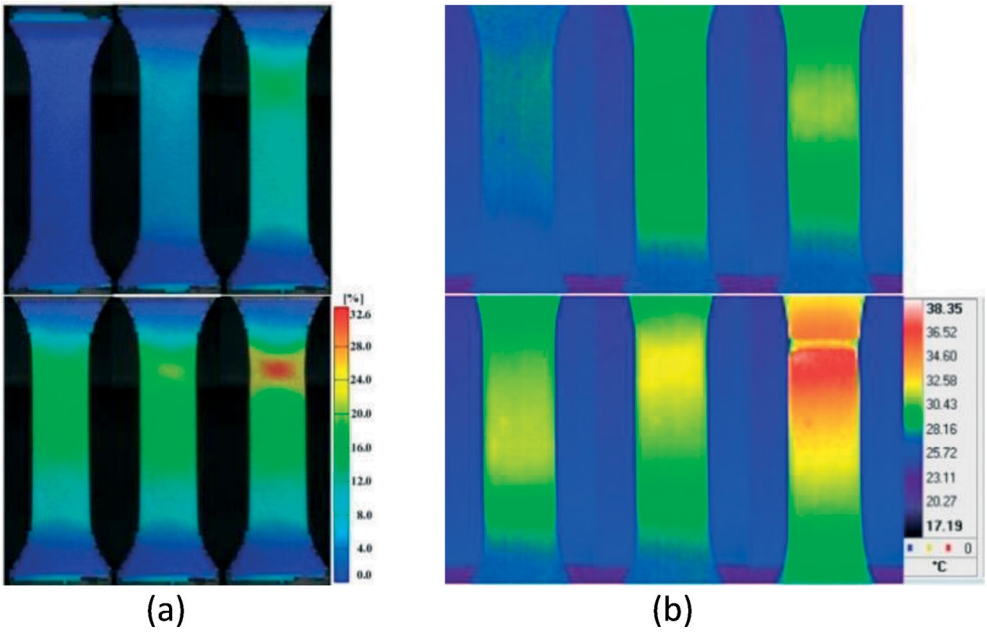

Fig. 2 – Displacement controlled tension test at 0.1 mm/s; (a) von Mises strain (3D DIC), (b) temperature distribution (IR) (Krstulović-Opara *et al.*, 2015)

Fig. 3 shows representative stress–strain hysteresis loops obtained from symmetrical tests ($\Delta\varepsilon/2=\pm1.2\%$) on a cylindrical specimen prepared according to ASTM E606 standard. It can be observed that the ductile nodular cast iron EN-GJS-400-18-LT exhibit significant cyclic hardening. Both types of material have a similar hardening rate and the major difference between them is in achieving maximum stress in first and all subsequent half-cycles as well as in achieving the first yielding point.

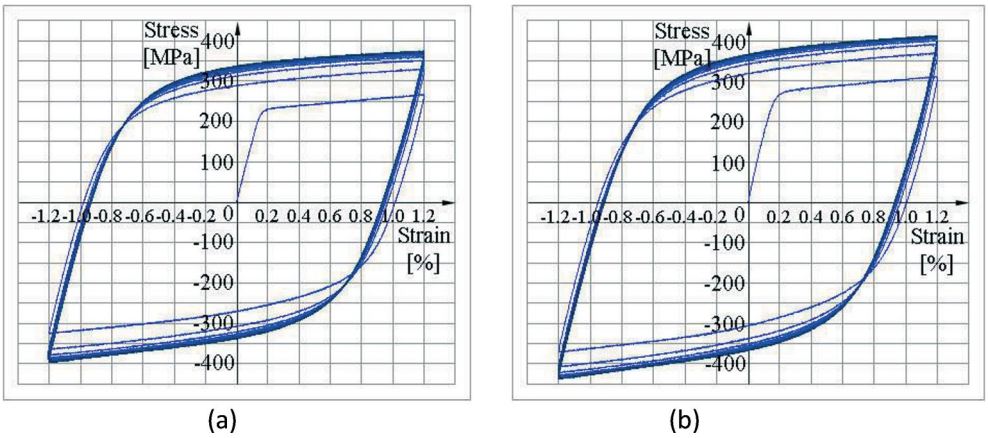

Fig. 3 – Stress–strain hysteresis loops for: (a) type 200 and (b) type 400 of the nodular cast iron (Čanžar, 2012; Čanžar, Tonković and Kodvanj, 2012)

The next part is concerned with the fatigue crack initiation and propagation testing on a compact tension (CT) specimen prepared according to ASTM E647 standard. Fig. 4 shows the cracked specimen with exposed nodular cast iron microstructure. As can be seen, the direction of crack growth is towards the graphite nodule which acts as a barrier for further crack propagation. The big advantage of nodular graphite are its round edges (despite the sharp edges of lamellar graphite) that not only reduces the risk of crack initiation, but also acts as a crack arrester and increases the crack propagation resistance. As it is described in (Ochi *et al.*, 2001), the fatigue cracks propagate in a zig–zag manner in the ferrite matrix but linearly in the pearlite matrix, because the difference in crack sensitivity depends on matrix strength and also because the ferrite grain boundary prevents crack propagation. In addition, fatigue cracks always start at the interface between the graphite nodule and the surrounding ferrite matrix, while graphite nodules remain generally unbroken (Bubenko, Konečná and Nicoletto, 2009).

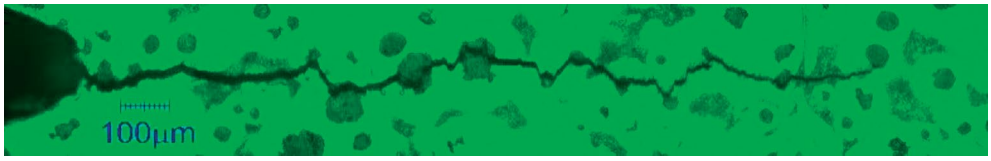

Fig. 4 – Microstructural crack exposure (Čanžar, 2012; Čanžar, Tonković and Kodvanj, 2012)

Fig. 5 illustrates the variation of the crack length (a) versus the number of cycles (N) for different load ratios (R). Herein, the test load is applied in sinusoidal form with the frequency of 10Hz, defined by the maximum load of 12kN and the load ratio R. The two different loading regimes (R=0.1 and R=0.5) for both material

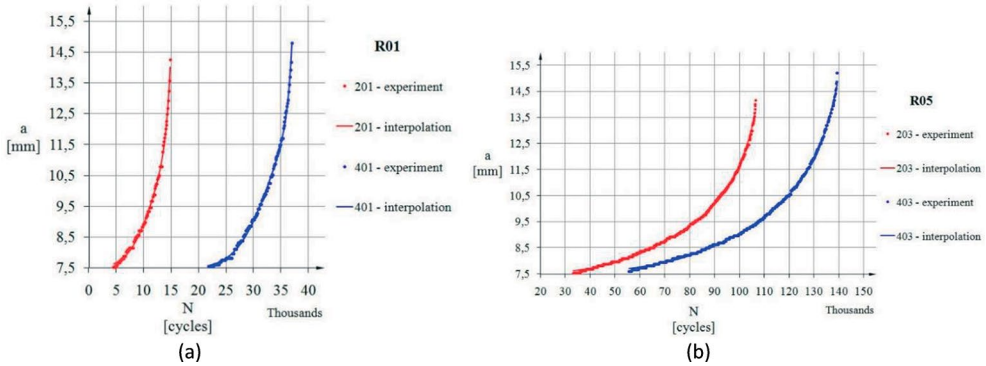

Fig. 5 – Number of cycles vs. crack length for: a) R=0.1 and b) R=0.5 load ratio (Čanžar, P., Tonković, Z., Bakić, A., Kodvanj, 2011)

types are performed. During the crack propagation tests, the crack length is measured in real time by an optical measuring system Aramis 4M using a novel technique proposed in (Čanžar, 2012; Čanžar, Tonković and Kodvanj, 2012). As expected, it has been observed that the number of cycles to failure increased with increase in load ratio. For the most rigorous load ratio R=0.1, there is the most pronounced difference in material types considering crack propagation. As described in (Čanžar, Tonković and Kodvanj, 2012), material type 200, produced by the flotret process, shows the least crack resistance. On the contrary, material type 400, produced by the inmould technique, lasts approximately 2.5 times longer till the final specimen fracture. The results show that the materials with a large number of smaller as well as with more regularly shaped graphite nodules and small ferrite grains (material types 300 and 400) have larger resistance to crack initiation and propagation resulting in higher fatigue life. A larger number of more regular and smaller nodules contributes more to higher fatigue resistance than a small number of large irregularly shaped graphite nodules that act as an internal notch in the ferritic matrix (material type 200). These results are consistent with those reported in (Iacoviello *et al.*, 2008; Xue, Bayraktar and Bathias, 2008; Hütter, Zybell and Kuna, 2015).

It can be concluded from the presented results that the size, shape and distribution of the graphite nodules have no significant influence on cyclic hardening of the ductile nodular cast iron EN-GJS-400-18-LT but they play a great role in the crack initiation and propagation process (Čanžar, 2012; Čanžar, Tonković and Kodvanj, 2012). This provided a motivation for research work in the field of deformation process modelling of heterogeneous materials using two-scale formulations ("macro-micro") based on the concepts of computational homogenization and RVE.

3. Numerical modelling of heterogeneous material

3.1 Basic relations of the nonlocal continuum

In addition to the strain tensor $\boldsymbol{\varepsilon}$ which is defined as a symmetric gradient of the displacement field $\mathbf{u}$ in the classical small strain continuum theory, the second-order strain $\boldsymbol{\eta}$ is introduced into the nonlocal continuum theory. $\boldsymbol{\eta}$ is the third-order tensor, representing the gradient of $\boldsymbol{\varepsilon}$

$$\boldsymbol{\eta} = \nabla \otimes \boldsymbol{\varepsilon} \,. \tag{1}$$

The variation of the strain energy density function is expressed as

$$\delta W = \frac{\partial W}{\partial \boldsymbol{\varepsilon}} : \delta \boldsymbol{\varepsilon} + \frac{\partial W}{\partial \boldsymbol{\eta}} : \delta \boldsymbol{\eta} = \boldsymbol{\sigma} : \delta \boldsymbol{\varepsilon} + \boldsymbol{\mu} : \delta \boldsymbol{\eta}. \tag{2}$$

In Eq. (2), $\boldsymbol{\sigma}$ and $\boldsymbol{\mu}$ represent the Cauchy and the double stress tensors, respectively, which are work conjugates to the strain and the second-order strain. Using straightforward mathematical manipulations, as explained in (Lesičar, Tonković and Sorić, 2014), relation (2) can be modified to

$$\delta W = \nabla \cdot \left(\boldsymbol{\sigma} \cdot \delta \mathbf{u}\right) - \left(\nabla \cdot \boldsymbol{\sigma}\right) \cdot \delta \mathbf{u} + \nabla \cdot \left[\boldsymbol{\mu} : \left(\nabla \otimes \left(\delta \mathbf{u}\right)\right)\right] - \nabla \cdot \left(\delta \mathbf{u} \cdot \left(\nabla \cdot \boldsymbol{\mu}\right)\right) + \left(\nabla \cdot \left(\nabla \cdot \boldsymbol{\mu}\right)\right) \cdot \delta \mathbf{u}. \tag{3}$$

From Eq. (3) the internal work variation can be defined in the integral form over the body surface A as

$$\begin{aligned} \delta W^{\text{int}} = & \int_A \left[\mathbf{n} \cdot \left(\boldsymbol{\sigma} - \left(\nabla \cdot \boldsymbol{\mu}\right)\right) \cdot \delta \mathbf{u}\right] \mathrm{d}A + \int_A \left[\left(\nabla^A \cdot \mathbf{n}\right) \otimes \mathbf{n} \cdot \left(\mathbf{n} \cdot \boldsymbol{\mu}\right) \cdot \delta \mathbf{u}\right] \mathrm{d}A - \\ & \int_A \left[\nabla^A \cdot \left(\mathbf{n} \cdot \boldsymbol{\mu}\right) \cdot \delta \mathbf{u}\right] \mathrm{d}A - \int_V \left[\nabla \cdot \left(\boldsymbol{\sigma} - \left(\nabla \cdot \boldsymbol{\mu}\right)\right) \cdot \delta \mathbf{u}\right] \mathrm{d}V + \int_A \left[\left(\mathbf{n} \cdot \boldsymbol{\mu} \cdot \mathbf{n}\right) \cdot \left(D \otimes \left(\delta \mathbf{u}\right)\right)\right] \mathrm{d}A, \end{aligned} \tag{4}$$

where the body forces are neglected. In Eq. (4), $\mathbf{n}$ represents unit outward normal, while ∇^A and D denote surface and normal gradient operators, respectively. The variation of the external work is written in the form

$$\delta W^{\text{ext}} = \int_A \left(\mathbf{t} \cdot \delta \mathbf{u}\right) \mathrm{d}A + \int_A \left[\boldsymbol{\tau} \cdot \left(D \otimes \left(\delta \mathbf{u}\right)\right)\right] \mathrm{d}A \,. \tag{5}$$

In Eq. (5), $\mathbf{t}$ and $\boldsymbol{\tau}$ are the surface traction and the double surface traction, respectively defined as

$$\mathbf{t} = \mathbf{n} \cdot \left(\boldsymbol{\sigma} - \left(\nabla \cdot \boldsymbol{\mu}\right)\right) + \left(\nabla^A \cdot \mathbf{n}\right) \otimes \mathbf{n} \cdot \left(\mathbf{n} \cdot \boldsymbol{\mu}\right) - \nabla^A \cdot \left(\mathbf{n} \cdot \boldsymbol{\mu}\right), \tag{6}$$

$$\boldsymbol{\tau} = \mathbf{n} \cdot \boldsymbol{\mu} \cdot \mathbf{n} \,. \tag{7}$$

The principle of virtual work is expressed by the relation

$$\delta W^{\text{int}} = \delta W^{\text{ext}} \tag{8}$$

which yields the equilibrium equation

$$\nabla \cdot \left(\boldsymbol{\sigma} - \left(\nabla \cdot \boldsymbol{\mu} \right) \right) = \mathbf{0} . \tag{9}$$

For more details on the derivation of the aforementioned relations, please refer to (Lesičar, Tonković and Sorić, 2012). Also, the presented relations can be easily extended to the large strain assumption, as derived in (Lesičar, Sorić and Tonković, 2016).

3.2 Finite element derivation

Within this research, the displacement-based C^1 continuous triangular finite element is derived and implemented into the FE software ABAQUS (ABAQUS, 2014). The C^1 continuity means that displacements and displacements derivatives within the element are continuous functions. The element is derived and adjusted for the application in the multiscale procedure. The proposed strain gradient triangular finite element is shown in Fig. 6.

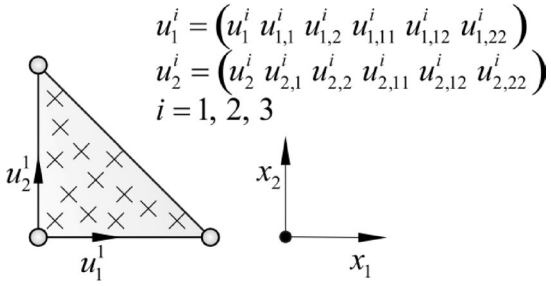

Fig. 6 – C^1 triangular finite element

The element consists of three nodes and twelve degrees of freedom (DOF) per node. The nodal degrees of freedom are two displacements and their first and second order derivatives with respect to the Cartesian coordinates. The element displacement field is approximated by the condensed fifth-order polynomial defined by 18 nodal values (Lesičar, Tonković and Sorić, 2012). The weak form of Eq. (9) expressed through the principle of virtual work may be presented as

$$\int_A \left(\boldsymbol{\sigma} : \delta\boldsymbol{\varepsilon} + \boldsymbol{\mu} \cdot \delta\boldsymbol{\eta} \right) \mathrm{d}A = \int_s \left(\mathbf{t} \cdot \delta\mathbf{u} \right) \mathrm{d}s + \int_s \left[\mathbf{T} : \left(\nabla \otimes \left(\delta\mathbf{u} \right) \right) \right] \mathrm{d}s , \tag{10}$$

where s represents the closed boundary line of the surface area A. Also, in the second integral term on the right side of (10), the double traction tensor $\mathbf{T} = \boldsymbol{\tau} \otimes \mathbf{n}$ is introduced. Due to the C^1 continuous interpolations adopted in the element formulation, only displacement field needs to be discretized, while the remaining gradient terms can be easily computed through the shape function derivatives. The displacement field $\mathbf{u}$ inside an element may be expressed by the well-known relation as

$$\mathbf{u} = \mathbf{N}\mathbf{v}\,. \tag{11}$$

In Eq. (11), $\mathbf{N}$ is the shape functions matrix, and $\mathbf{v}$ is the vector of the nodal degrees of freedom. The strain $\boldsymbol{\varepsilon}$ and the higher-order displacement gradient $\boldsymbol{\eta}$ are obtained by the shape function derivatives using the following relations

$$\boldsymbol{\varepsilon} = \begin{bmatrix} \varepsilon_{11} \\ \varepsilon_{22} \\ 2\varepsilon_{12} \end{bmatrix} = \mathbf{B}_{\varepsilon}\mathbf{v}\,, \tag{12}$$

$$\boldsymbol{\eta} = \begin{bmatrix} \eta_{111} \\ \eta_{222} \\ \eta_{221} \\ \eta_{112} \\ 2\eta_{121} \\ 2\eta_{212} \end{bmatrix} = \begin{bmatrix} u_{1,11} \\ u_{2,22} \\ u_{1,22} \\ u_{2,11} \\ 2u_{1,21} \\ 2u_{2,12} \end{bmatrix} = \mathbf{B}_{\eta}\mathbf{v}\,, \tag{13}$$

where $\mathbf{B}_{\varepsilon}$ and $\mathbf{B}_{\eta}$ are the matrices containing appropriate interpolation polynomials derivatives. Since in a general case, the material and geometrical nonlinearities may be involved, relation (10) should be solved in an incrementally-iterative procedure via iterative corrections. Therefore, the constitutive updates of the stress and double stress are computed by the linearized incremental constitutive relations

$$\Delta\boldsymbol{\sigma} = \mathbf{C}_{\sigma\varepsilon} : \Delta\boldsymbol{\varepsilon} + \mathbf{C}_{\sigma\eta} : \Delta\boldsymbol{\eta}\,, \tag{14}$$

$$\Delta\boldsymbol{\mu} = \mathbf{C}_{\mu\varepsilon} : \Delta\boldsymbol{\varepsilon} + \mathbf{C}_{\mu\eta} : \Delta\boldsymbol{\eta}\,. \tag{15}$$

Herein $\mathbf{C}_{\sigma\varepsilon}$, $\mathbf{C}_{\sigma\eta}$, $\mathbf{C}_{\mu\varepsilon}$ and $\mathbf{C}_{\mu\eta}$ are the consistent material tangent stiffness matrices providing correlations among corresponding stress and strain variables. Using the standard finite element mathematical procedures, the usual linearized finite element equation is obtained

$$\mathbf{K}\mathbf{v} = \mathbf{F}_{\mathrm{e}} - \mathbf{F}_{\mathrm{i}}\,. \tag{16}$$

More details about derivation of the finite element and element matrices used in Eq. (16) can be found in the authors' publication (Lesičar, Tonković and Sorić, 2014) for the small strain case, as well as in (Lesičar, Sorić and Tonković, 2016) for the large strain assumption. However, in the present contribution, a special case of the strain gradient theory was adopted (Aifantis, 1999). Accordingly, the modified constitutive relations are used, where the stress tensors are defined as

$$\Delta\boldsymbol{\sigma} = \mathbf{C} : \Delta\boldsymbol{\varepsilon}\,, \tag{17}$$

$$\Delta\boldsymbol{\mu}_{x_1} = l^2 \left(\mathbf{C} : \Delta\boldsymbol{\varepsilon}_{x_1} \right), \tag{18}$$

$$\Delta\boldsymbol{\mu}_{x_2} = l^2 \left(\mathbf{C} : \Delta\boldsymbol{\varepsilon}_{x_2} \right). \tag{19}$$

In the constitutive relations (18) and (19), $\boldsymbol{\varepsilon}_{x_1}$ and $\boldsymbol{\varepsilon}_{x_2}$ represent strain gradients with respect to the Cartesian coordinates x_1 and x_2, while $\boldsymbol{\mu}_{x_1}$ and $\boldsymbol{\mu}_{x_2}$ are their work conjugates. As can be seen, they are multiplied by the material dependent microstructural parameter l. For more details, see (Akarapu and Zbib, 2006).

4. Two scale transitions and homogenization

All materials can be considered as heterogeneous at various scales of observation. Material heterogeneities are interesting ultimately through their influence on non-uniform response and microstructure evolution. Using the multiscale setting, the constitutive models applicable at engineering scales can be developed using detailed information obtained from finer scales through application of newly developed class of computational homogenization methods. The computational homogenization allows incorporation of the microstructure into a standard continuum model turning standard boundary value problem into a nested boundary value problem, containing both the macroscale and the microscale level. The macroscopic properties are determined by the homogenization process acting on the effective, homogenized sample of material called RVE. The resulting effective material is supposed to represent all macroscopic properties of the microheterogeneous structure and enables to restrict the computational effort to the smallest, still representative, material sample. In the presented scheme, the microstructure is described by the strain gradient elasticity theory assuming linear elastic material behaviour and small strains. In the following the subscript "m" is appointed to microlevel variables and the subscript "M" represents macrolevel quantities.

4.1 Macro to micro scale transition

The starting point in the macro-to-micro transition is a Taylor series expansion of the RVE displacement field depending on the macroscale displacement gradients (Geers and Kouznetsova, 2010) expressed as

$$\mathbf{u}_{\mathrm{m}} = \boldsymbol{\varepsilon}_{\mathrm{M}} \cdot \mathbf{x} + \frac{1}{2}\left[\mathbf{x} \cdot \left(\nabla \otimes \boldsymbol{\varepsilon}_{\mathrm{M}}\right) \cdot \mathbf{x}\right] + \mathbf{r}\,. \tag{20}$$

In Eq. (20), $\mathbf{r}$ represents the microfluctuation displacement field. The microfluctuations are short-wavelength displacements representing a contribution of the microconstituents to the macrolevel displacement field. Since in the multiscale scheme the microstructure is explicitly modelled, the contribution of the microfluctuations should be accounted for. As known in the homogenization theory, the volume average of the microscale quantities must be equal to their macroscale conjugates at a material point. Enforcing this principle between the macrolevel and microlevel strains, and the second-order strains as well, the following microfluctuation constraints arise

$$\frac{1}{V}\int_{V}\left(\nabla_{\mathrm{m}} \otimes \mathbf{r}\right)\mathrm{d}V = \frac{1}{V}\int_{\Gamma}\left(\mathbf{n} \otimes \mathbf{r}\right)\mathrm{d}\Gamma = \mathbf{0}\,, \tag{21}$$

$$\frac{1}{V}\int_{V}\left(\nabla_{\mathrm{m}} \otimes \left(\nabla_{\mathrm{m}} \otimes \mathbf{r}\right)\right)\mathrm{d}V = \frac{1}{V}\int_{\Gamma}\left(\mathbf{n} \otimes \left(\nabla_{\mathrm{m}} \otimes \mathbf{r}\right)\right)\mathrm{d}\Gamma = \mathbf{0}\,, \tag{22}$$

where G represents the RVE boundary, as shown in Fig. 7. Enforcement of the constraints (21) and (22) is easily achieved by means of the appropriate boundary conditions used on the RVE. In this research the gradient displacement- and gradient generalized periodic boundary conditions will be utilized. Since in the case of gradient displacement boundary conditions the microfluctuation field on the RVE boundaries is suppressed, (21) and (22) are satisfied without any actions. In the case of periodicity assumption, see (Geers and Kouznetsova, 2010), it is easy to prove that (21) and (22) are fulfilled. In the finite element context, Eq. (20) should be rewritten in matrix form to express the nodal degrees of freedom of an ith node along the RVE boundaries, which gives the following identity

$$\mathbf{u}_i = \mathbf{D}_i^T \boldsymbol{\varepsilon}_{\mathrm{M}} + \left(\mathbf{H}_1^T\right)_i \left(\boldsymbol{\varepsilon}_{,1}\right)_{\mathrm{M}} + \left(\mathbf{H}_2^T\right)_i \left(\boldsymbol{\varepsilon}_{,2}\right)_{\mathrm{M}}\,. \tag{23}$$

In Eq. (23), the macrolevel strains and strain gradients have the form according to the gradient theory adopted in the homogenization scheme. $\mathbf{D}$, $\mathbf{H}_1$ and $\mathbf{H}_2$ are the coordinate matrices which transform strains into finite element nodal degrees of freedom (Lesičar and Tonković, 2015).

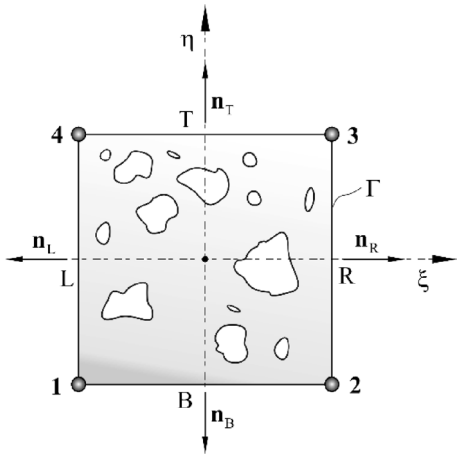

Fig. 7 – Representative Volume Element

Based on (20) and (23), the microfluctuation constraints (21) and (22) can be rearranged to

$$\int_\Gamma \mathbf{u}_\Gamma \, \mathrm{d}\Gamma = \left(\int_\Gamma \mathrm{D}_\Gamma^T \, \mathrm{d}\Gamma \right) \boldsymbol{\varepsilon}_\mathrm{M} + \left(\int_\Gamma \left(\mathbf{H}_1^T \right)_\Gamma \mathrm{d}\Gamma \right) \left(\boldsymbol{\varepsilon}_{,1} \right)_\mathrm{M} + \left(\int_\Gamma \left(\mathbf{H}_2^T \right)_\Gamma \mathrm{d}\Gamma \right) \left(\boldsymbol{\varepsilon}_{,2} \right)_\mathrm{M} . \quad (24)$$

By imposition of (23) and (24) on the RVE, the boundary value problem of the RVE is fully settled. A corresponding solution can be found by any appropriate technique, mostly the finite element method.

4.2 Micro to macro scale transition

After resolving the microlevel boundary value problem, the stress tensors and the constitutive behaviour are required for the macroscale computation. In the scale transition, the energy equivalence principle is fulfilled through the Hill-Mandel condition

$$\frac{1}{V} \int_V \left(\boldsymbol{\sigma}_\mathrm{m} : \delta\boldsymbol{\varepsilon}_\mathrm{m} + \boldsymbol{\mu}_\mathrm{m} : \left(\nabla_\mathrm{m} \otimes \delta\boldsymbol{\varepsilon}_\mathrm{m} \right) \right) \mathrm{d}V = \boldsymbol{\sigma}_\mathrm{M} : \delta\boldsymbol{\varepsilon}_\mathrm{M} + \boldsymbol{\mu}_\mathrm{M} : \left(\nabla \otimes \delta\boldsymbol{\varepsilon}_\mathrm{M} \right) . \quad (25)$$

Obviously, for further derivation, relation (20) can be inserted into Eq. (25). After a lengthy procedure, which is explained in (Lesičar, Tonković and Sorić, 2017), one can obtain homogenized stress tensors relations

$$\boldsymbol{\sigma}_\mathrm{M} = \frac{1}{V} \int_V \boldsymbol{\sigma}_\mathrm{m} \, \mathrm{d}V , \quad (26)$$

$$\boldsymbol{\mu}_\mathrm{M} = \frac{1}{V} \int_V \left(\boldsymbol{\mu}_\mathrm{m} + \boldsymbol{\sigma}_\mathrm{m} \otimes \mathbf{x} \right) \mathrm{d}V . \quad (27)$$

To complete the whole micro-macro procedure, the macroscopic constitutive behaviour is necessary. Since the heterogeneous materials are considered, the constitutive relations are much more complex compared to the usual forms used for homogeneous materials. Due to the irregular microstructure which is accounted for, the stresses depend not only on their energy conjugate strains, but also on the other displacement gradients appearing in the numerical model. Hence, to account the contribution of the heterogeneous microstructure on the macroscale, the generalized constitutive relations are derived in which every stress tensor is expressed in terms of the macrolevel displacement gradient tensors, as

$$\begin{aligned}
\Delta\boldsymbol{\sigma}_{\mathrm{M}} &= \mathbf{C}_{\sigma\varepsilon} : \Delta\boldsymbol{\varepsilon}_{\mathrm{M}} + \mathbf{C}_{\sigma\varepsilon_{x_1}} : \Delta\left(\boldsymbol{\varepsilon}_{,1}\right)_{\mathrm{M}} + \mathbf{C}_{\sigma\varepsilon_{x_2}} : \Delta\left(\boldsymbol{\varepsilon}_{,2}\right)_{\mathrm{M}}, \\
\Delta\left(\boldsymbol{\mu}_{x_1}\right)_{\mathrm{M}} &= \mathbf{C}_{\mu_{x_1}\varepsilon} : \Delta\boldsymbol{\varepsilon}_{\mathrm{M}} + \mathbf{C}_{\mu_{x_1}\varepsilon_{x_1}} : \Delta\left(\boldsymbol{\varepsilon}_{,1}\right)_{\mathrm{M}} + \mathbf{C}_{\mu_{x_1}\varepsilon_{x_2}} : \Delta\left(\boldsymbol{\varepsilon}_{,2}\right)_{\mathrm{M}}, \\
\Delta\left(\boldsymbol{\mu}_{x_2}\right)_{\mathrm{M}} &= \mathbf{C}_{\mu_{x_2}\varepsilon} : \Delta\boldsymbol{\varepsilon}_{\mathrm{M}} + \mathbf{C}_{\mu_{x_2}\varepsilon_{x_1}} : \Delta\left(\boldsymbol{\varepsilon}_{,1}\right)_{\mathrm{M}} + \mathbf{C}_{\mu_{x_2}\varepsilon_{x_2}} : \Delta\left(\boldsymbol{\varepsilon}_{,2}\right)_{\mathrm{M}}.
\end{aligned} \tag{28}$$

Accordingly, the nine constitutive operators are required. They are derived by the static condensation procedure of the global RVE stiffness, as explained in (Lesičar, Tonković and Sorić, 2017). The homogenized constitutive matrices are expressed through the condensed RVE stiffness $\tilde{\mathbf{K}}_{\mathrm{bb}}$ and the coordinate matrices as

$$\begin{aligned}
&\mathbf{C}_{\sigma\varepsilon} = \frac{1}{V}\mathbf{D}\tilde{\mathbf{K}}_{\mathrm{bb}}\mathbf{D}^T, \quad \mathbf{C}_{\sigma\varepsilon_{x_1}} = \frac{1}{V}\mathbf{D}\tilde{\mathbf{K}}_{\mathrm{bb}}\mathbf{H}_1^T, \quad \mathbf{C}_{\sigma\varepsilon_{x_2}} = \frac{1}{V}\mathbf{D}\tilde{\mathbf{K}}_{\mathrm{bb}}\mathbf{H}_2^T, \\
&\mathbf{C}_{\mu_{x_1}\varepsilon} = \frac{1}{V}\mathbf{H}_1\tilde{\mathbf{K}}_{\mathrm{bb}}\mathbf{D}^T, \quad \mathbf{C}_{\mu_{x_1}\varepsilon_{x_1}} = \frac{1}{V}\mathbf{H}_1\tilde{\mathbf{K}}_{\mathrm{bb}}\mathbf{H}_1^T, \quad \mathbf{C}_{\mu_{x_1}\varepsilon_{x_2}} = \frac{1}{V}\mathbf{H}_1\tilde{\mathbf{K}}_{\mathrm{bb}}\mathbf{H}_2^T, \\
&\mathbf{C}_{\mu_{x_2}\varepsilon} = \frac{1}{V}\mathbf{H}_2\tilde{\mathbf{K}}_{\mathrm{bb}}\mathbf{D}^T, \quad \mathbf{C}_{\mu_{x_2}\varepsilon_{x_1}} = \frac{1}{V}\mathbf{H}_2\tilde{\mathbf{K}}_{\mathrm{bb}}\mathbf{H}_1^T, \quad \mathbf{C}_{\mu_{x_2}\varepsilon_{x_2}} = \frac{1}{V}\mathbf{H}_2\tilde{\mathbf{K}}_{\mathrm{bb}}\mathbf{H}_2^T.
\end{aligned} \tag{29}$$

4.3 Numerical implementation

The multiscale procedure comprising the presented nonlocal homogenization scheme was implemented in the commercial software ABAQUS, as shown in Fig. 8. The C^1 finite element formulation is used for discretization at both the macroscale and the microscale. Since the C^1 finite elements are not supported by the Abaqus finite element library, the element developed was implemented by means of the user subroutine UEL. Even though the same finite element is used at both scales, there are some differences in their formulation. As mentioned before, at the macrolevel the global nonlinear finite element equation is solved. In each material point of the macrolevel element, the displacement gradient increments $\Delta\boldsymbol{\varepsilon}_{\mathrm{M}}$, $\Delta(\boldsymbol{\varepsilon}_{,1})_{\mathrm{M}}$ and $\Delta(\boldsymbol{\varepsilon}_{,2})_{\mathrm{M}}$ are computed and updated. Afterwards, they are prescribed on the RVE boundaries in the form of the RVE boundary conditions based on relation (23). At the microlevel, the boundary value problem is solved, where the homoge-

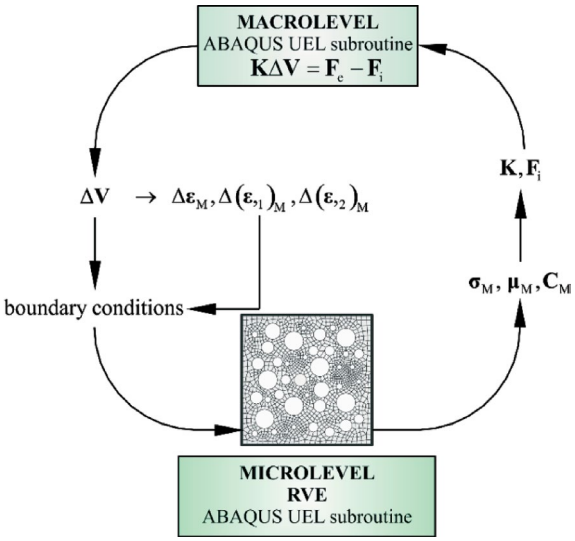

Fig. 8 – Micro-macro multiscale algorithm

nization procedure is conducted by means of Eqs. (26), (27) and (29). After solving the RVE boundary value problem using the derived homogenization strategy, the results are transferred back to the macrolevel material point. The presented computational procedure must be carried out at every finite element integration point. For more details about implementation, see (Lesičar, Tonković and Sorić, 2017).

5. Numerical example

The presented procedure is verified on a problem of three-point bending test of the notched specimen. The deformed discretized model with boundary conditions is presented in Fig. 9. The dimensions of the test specimen are 100 × 20 × 10 mm with a notch root radius of 0.08 mm according to standard ASTM E1820. The support-span is 79 mm.

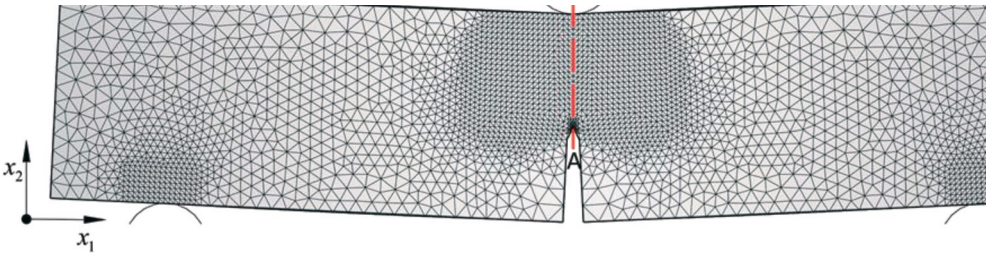

Fig. 9 – Three-point bending test specimen

The boundary conditions are suited as the simulation of a real experimental setup. The support span is modelled as two support rollers with a diameter of 8 mm. The force of 10 kN was applied over the loading roller. The rollers are modelled as rigid bodies. The finer mesh is used in the vicinity of the notch (Fig. 10) and near the roller contact regions, where the high stress gradient is expected. Since at the moment the authors do not possess necessary data of the RVE representing the nodular cast iron, the material considered is an academic example of the linear elastic steel with 13% randomly distributed porosities. However, this academic material is the closest representation of real nodular iron. The Young's modulus is taken as 210 GPa, which describes the ferritic matrix and the Poisson's ratio is set to 0.3. The porosities represent graphite nodules, which are not explicitly modelled here due to their negligible stiffness in comparison to the matrix material. The material microstructure is represented by the RVE1 of the side length $L = 0.2$ mm discretized by 790 finite elements as shown in Fig. 11. On the RVE, the gradient generalized periodic boundary conditions were used.

The constant discretization mesh was kept along the red line A-A displayed in Fig. 9. The analysis of this problem was conducted in an adaptive manner. The material constitutive matrices are computed by the homogenization prior to the analysis. For the linear elastic problem considered here the homogenized stress tensors values can be obtained by the analytical expression in a standard manner. For the generalized constitutive behaviour due to the analysis of the heterogeneous material the stress tensors are then calculated according to relations (28). The adaptivity mentioned here means that a few elements in front of the notch inside the red line in Fig. 10 are computed in the multiscale setting attaching the RVE1 to their material points in order to track the microstructural effects in front of the notch.

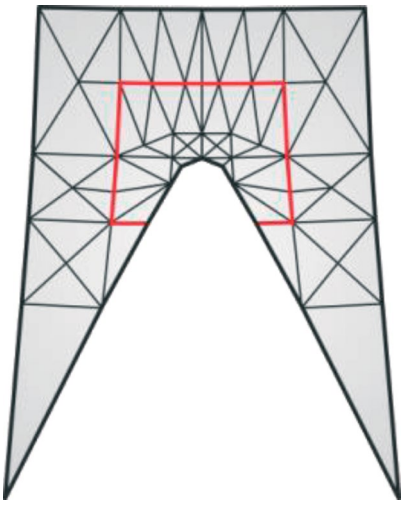

Fig. 10 – Mesh around notch root

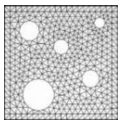

Fig. 11 – RVE1

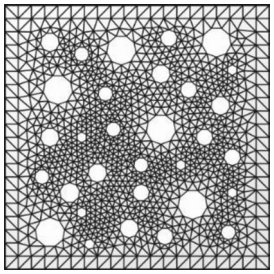

Fig. 12 – RVE2

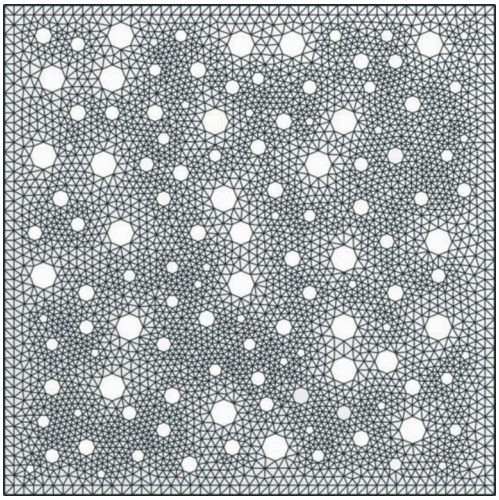

Fig. 13 – RVE3

In order to prove that the microstructure presented in Fig. 11 is truly representative, two larger RVEs, the RVE2 with side length L = 0.5mm and the RVE3 with side length L = 1mm were considered, too. Their geometries are shown in Figs. 12 and 13. However, in the second-order homogenization, the RVE size directly involves managing of the nonlocality effects. Thus, for the comparison of the results all the RVE sizes needed to describe the same nonlocal behaviour were governed by the same nonlocal parameter. To ensure comparability, the appropriate combination of the RVE size and microstructural parameter l was chosen, as briefly discussed in (Lesičar, Tonković and Sorić, 2017). For both larger RVE sizes the same behaviour of the specimen is exhibited, which leads to the conclusion that the microstructural model represented in Fig. 11 can be found as a true RVE. In the following figures the distribution of the relevant displacement gradient in front of the notch along the line A-A of length H = 11mm is presented. For the bending pattern exhibited here the dominant gradients of displacements are $u_{1,1}$ which is in fact the strain ε_{11}, and opens the notch, $u_{1,21}$ describing the trapezoidal deformed shape and $u_{2,11}$ representing curvature. The multiple analyses were conducted for various values of the microstructural parameter l. Figs. 14, 16 and 18 show the distributions of the relevant displacement gradients in front of the notch. In these diagrams the ordinate represents the distance from the notch tip in the vertical direction denoted as H. As expected, the high gradients appear in the vicinity of the notch due to the geometrical discontinuity and on the upper surface of the specimen due to the roller penetration causing crimping of the material. Moving away from the notch tip the peak areas the gradients rapidly drop and disappear in the inner part of the specimen. With an increase in l the general behaviour is preserved, but the stiffness of the material is increased due to a larger nonlocal influence. Detailed insight into the distributions in front of the notch are given in Figs. 15, 17, and 19. It is visible that the stiffer

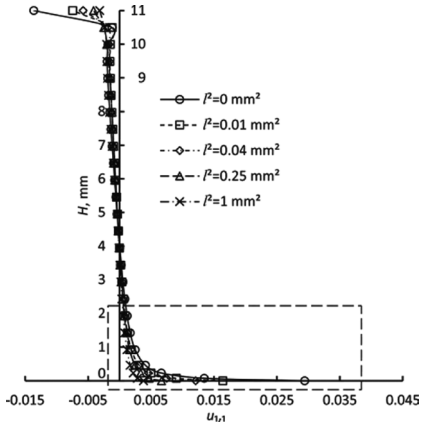

Fig. 14 – Distribution of $u_{1,1}$ in front of the notch

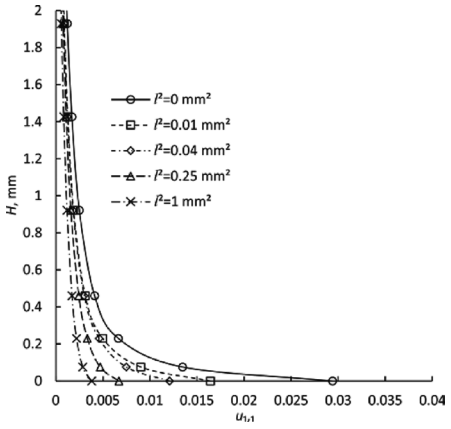

Fig. 15 – Detail of distribution of $u_{1,1}$ in front of the notch

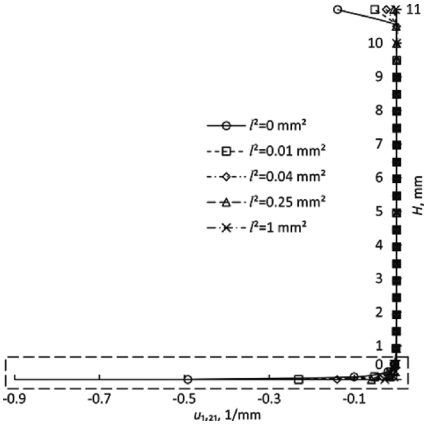

Fig. 16 – Distribution of $u_{1,21}$ in front of the notch

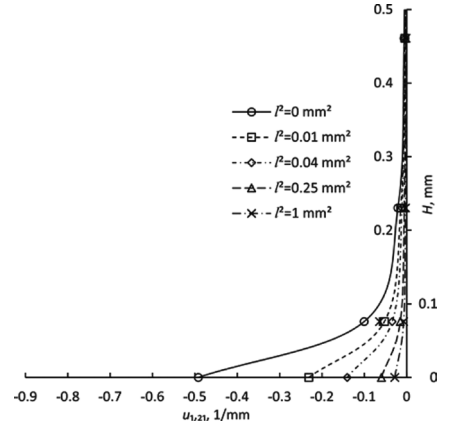

Fig. 17 – Detail of distribution of $u_{1,21}$ in front of the notch

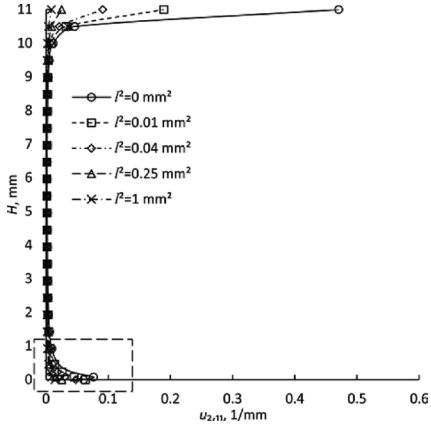

Fig. 18 – Distribution of $u_{2,11}$ in front of the notch

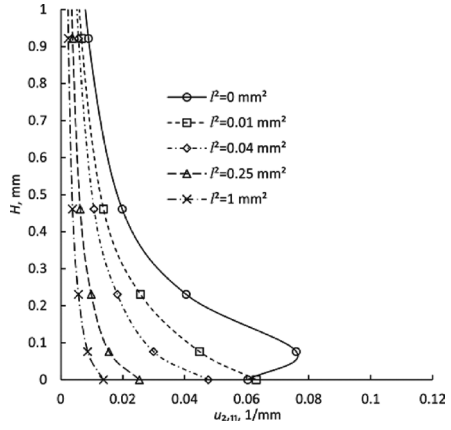

Fig. 19 – Detail of distribution of $u_{2,11}$ in front of the notch

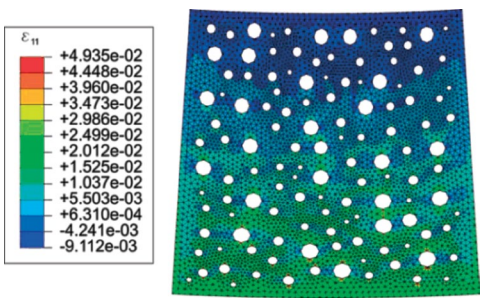

Fig. 20 – Distribution of ε_{11} on RVE3

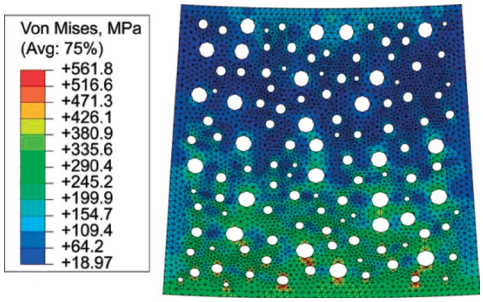

Fig. 21 – Distribution of Von Mises stress on RVE3

response coming with increased l is common to all gradients. Furthermore, Figs. 20 and 21 displays the strain ε_{11} and the Von Mises stress on the RVE3 located at the notch tip for $l^2 = 0$. On this RVE the gradient displacement boundary conditions are utilized. It can be seen that the RVE is elongated as a consequence of ε_{11}. Due to the mixed second-order derivative $u_{1,21}$, the trapezoidal deformation mode is prominent. The curvature, which is the result of $u_{2,11}$ is not expressed in such an extent as the trapezoidal mode, but with a further increase in loading it could be easily distinguished. In Fig. 20 a smooth change of strain from tension to compression is visualized, as expected for the bending problem. The distribution of the equivalent Von Mises stress is visualized in Fig. 21, which is exhibited in accordance to the deformation mode. Also, stress concentrations around pores representing the graphite nodules can be observed. As is known, t stress concentrations serve as initiators of a damage and may cause further softening of materials. In future research, an extension of the material behaviour towards softening will be considered, where the influence of stress concentration on damage initiation and propagation at the microlevel will be studied.

6. Conclusion

The paper presents an approach for numerical modelling of deformation responses of heterogeneous engineering materials. Nodular cast iron, which is widely used in engineering structural components, is described in more detail. It is shown that its heterogeneity described by size, shape and distribution of the graphite nodules has significant influence on load carrying capacity. The numerical analysis requires the consideration at both macro- and microscale which may be performed by means of a multiscale approach.

In this contribution the second-order two-scale computational homogenization scheme employing the strain gradient elasticity theory at the macro- and microlev-

el is presented. The formulation of the nonlocal theory is embedded into the finite element framework using the C^1 continuity three node triangular plane strain finite element. It is shown that the two-scale formulation applied is mathematically more consistent than the multiscale approach using the nonlocal theory only at the macrolevel, usually used in available literature.

All algorithms developed are implemented in the FE software ABAQUS. To demonstrate the capability of the presented computational procedure, the three-point bending test of the notched specimen was modelled. The microstructure of the nodular cast iron is presented by the academics RVEs. The influence of the RVE size as well as the microstructural parameter on the material behaviour are analysed and discussed. As expected, the realistic deformation responses are computed.

Further research should be directed to the application of the presented algorithm to the more realistic description of nodular cast iron microstructure. In addition, some damage phenomena at the microstructural level should be modelled, which can lead to fracture development at the material point of the macroscale. An accurate and numerically efficient damage and fracture modelling can significantly contribute to the assessment of structural integrity and lifetime prediction as well.

Acknowledgement. This work has been fully supported by Croatian Science Foundation under the project "Multiscale Numerical Modelling of Material Deformation Responses from Macro- to Nanolevel" (2516).

References

ABAQUS (2014) 'ABAQUS/Standard', ABAQUS. 6.14-1. Providence, RI, USA: Dassault Systemes. Aifantis, E. C. (1999) 'Strain gradient interpretation of size effects', International Journal of Fracture. Kluwer Academic Publishers, 95(1–4), pp. 299–314.

Akarapu, S. and Zbib, H. (2006) 'Numerical analysis of plane cracks in strain-gradient elastic materials', International Journal of Fracture. Kluwer Academic Publishers, 141(3–4), pp. 403–430.

Amanatidou, E. and Aravas, N. (2002) 'Mixed finite element formulations of strain-gradient elasticity problems', Computer Methods in Applied Mechanics and Engineering, 191, pp. 1723–1751.

Argyris, J. H., Fried, I. and Scharpf, D. W. (1968) The TUBA family of plate elements for the matrix displacement method.

Askes, H., Bennett, T. and Aifantis, E. C. (2007) 'A new formulation and C0-implementation of dynamically consistent gradient elasticity', International Journal for Numerical Methods in Engineering. John Wiley & Sons, Ltd., 72(1), pp. 111–126.

de Borst, R., Pamin, J. and Geers, M. G. D. (1999) 'On coupled gradient-dependent plasticity and damage theories with a view to localization analysis', European Journal of Mechanics - A/Solids, 18(6), pp. 939–962.

Britta Hirschberger, C., Kuhl, E. and Steinmann, P. (2007) 'On deformational and configurational mechanics of micromorphic hyperelasticity – Theory and computation', Computer Methods in Applied Mechanics and Engineering, 196(41–44), pp. 4027–4044.

Bubenko, L., Konečná, R. and Nicoletto, G. (2009) 'Observation of Fatigue Crack Paths in Nodular Cast Iron and ADI Microstructures', Materi. Ing., pp. 13–18.

Clough, R. and Tocher, J. (1965) 'Finite element stiffness matrices for analysis of platebending', Finite element stiffness matrices for analysis of plate bending, pp. 515–545.

Cosserat, E. and Cosserat, F. (1909) 'Théorie des Corps déformables', Nature, 81(2072), p. 67. Costa, N., Machado, N. and Silva, F. S. (2008) 'Influence of Graphite Nodules Geometrical Features on Fatigue Life of High-Strength Nodular Cast Iron', Journal of Materials Engineering and Performance, 17(3), pp. 352–362.

Costa, N., Machado, N. and Silva, F. S. (2010) 'A new method for prediction of nodular cast iron fatigue limit', International Journal of Fatigue. Elsevier, 32(7), pp. 988–995.

Čanžar, P., Tonković, Z., Bakić, A., Kodvanj, J. (2011) 'Experimental and Numerical Investigation of Fatigue Behaviour of Nodular Cast Iron for Wind Turbine Applications', Key Engineering Materials, 488–189, pp. 182–185.

Čanžar, P. and Tonković, Z. (2014) 'Nodular Cast Iron – Fatigue Crack Measurement and Simulation', Key Engineering Materials, 577–578, pp. 473–473.

Čanžar, P. (2012) Experimental and numerical modelling of fatigue behavior of nodular cast iron. University of Zagreb.

Čanžar, P., Tonković, Z. and Kodvanj, J. (2012) 'Microstructure influence on fatigue behaviour of nodular cast iron', Materials Science and Engineering: A, 556(0), pp. 88–99.

Fischer, P. E., Steinmann, P. D.-I. habil. P. and Willner, P. D.-I. habil. K. (2011) C^1 Continuous Methods in ComputationalGradient Elasticity, Lehrstuhl fur Technische Mechanik. University Erlangen-Nurnberg.

Fleck, N. A. and Hutchinson, J. W. (1993) 'A phenomenological theory for strain gradient effects in plasticity', Journal of the Mechanics and Physics of Solids, 41(12), pp. 1825–1857.

Fleck, N. A. and Hutchinson, J. W. (2001) 'A reformulation of strain gradient plasticity', Journal of the Mechanics and Physics of Solids, 49(10), pp. 2245–2271.

Geers, M. G. D. and Kouznetsova, V. G. (2010) Scale transitions in solid mechanics based on computational homogenization. Eindhoven: Eindhoven University of Technology.

Germain, P. (1973) 'The Method of Virtual Power in Continuum Mechanics. Part 2: Microstructure', SIAM Journal on Applied Mathematics, 25(3), pp. 556–575.

Gitman, I. M., Gitman, M. B. and Askes, H. (2006) 'Quantification of stochastically stable representative volumes for random heterogeneous materials', Archive of Applied Mechanics. Springer-Verlag, 75(2–3), pp. 79–92.

Hübner, P. et al. (2007) 'Load history effects in ductile cast iron for wind turbine components', International Journal of Fatigue. Elsevier, 29(9–11), pp. 1788–1796.

Hütter, G., Zybell, L. and Kuna, M. (2015) 'Micromechanisms of fracture in nodular cast iron: From experimental findings towards modeling strategies – A review', Engineering Fracture Mechanics. Pergamon, 144, pp. 118–141.

Iacoviello, F. et al. (2008) 'Damaging micromechanisms in ferritic–pearlitic ductile cast irons', Materials Science and Engineering: A. Elsevier, 478(1–2), pp. 181–186.

Koiter, W. (1963) Couple-stresses in the theory of elasticity.

Krstulović-Opara, L. et al. (2015) 'Comparison of infrared and 3D digital image correlation techniques applied for mechanical testing of materials', Infrared Physics & Technology. Pergamon, 73, pp. 166–174.

Lesičar, T., Sorić, J. and Tonković, Z. (2016) 'Large strain, two-scale computational approach using C^1 continuity finite element employing a second gradient theory', Computer Methods in Applied Mechanics and Engineering, 298.

Lesičar, T. and Tonković, Z. (2015) Multiscale Modeling of Heterogeneous Materials Using Second-Order Homogenization, Faculty of Mechanical Engineering and Naval Architecture. University of Zagreb.

Lesičar, T., Tonković, Z. and Sorić, J. (2012) 'C^1 Continuity Finite Element Formulation in Second-Order Computational Homogenization Scheme', Journal of Multiscale Modelling, 4(4), p. 1250013.

Lesičar, T., Tonković, Z. and Sorić, J. (2014) 'A second-order two-scale homogenization procedure using C^1 macrolevel discretization', Computational Mechanics, 54(2).

Lesičar, T., Tonković, Z. and Sorić, J. (2017) 'Two-scale computational approach using strain gradient theory at microlevel', International Journal of Mechanical Sciences, 126.

Luscher, D. J., McDowell, D. L. and Bronkhorst, C. A. (2010) 'A second gradient theoretical sframework for hierarchical multiscale modeling of materials', International Journal of Plasticity, 26(8), pp. 1248–1275.

Maugin, G. A. and Metrikine, A. V (2010) Mechanics of Generalized Continua, Advances in Mechanics and Mathematics. Edited by G. A. Maugin and A. V Metrikine. Springer.

Mindlin, R. D. (1965) 'Second gradient of strain and surface-tension in linear elasticity', International Journal of Solids and Structures, 1(4), pp. 417–438.

Mindlin, R. D. and Tiersten, H. F. (1962) 'Effects of couple-stresses in linear elasticity', sArchive for Rational Mechanics and Analysis. Springer-Verlag, 11(1), pp. 415–448.

Minnebo, P., Nilsson, K.-F. and Blagoeva, D. (2007) 'Tensile, Compression and Fracture Properties of Thick-Walled Ductile Cast Iron Components', Journal of Materials Engineering and Performance, 16(1), pp. 35–45.

Ochi, Y. et al. (2001) 'Effect of shot-peening treatment on high cycle fatigue property of ductile cast iron', International Journal of Fatigue. Elsevier, 23(5), pp. 441–448.

Putar, F. et al. (2017) 'Damage modeling employing strain gradient continuum theory', International Journal of Solids and Structures, 120.

Ru, C. and Aifantis, E. (1993) 'A simple approach to solve boundary-value problems in gradient elasticity', Acta Mechanica, pp. 59–68.

Shirani, M. and Härkegård, G. (2011) 'Fatigue life distribution and size effect in ductile cast siron for wind turbine components', Engineering Failure Analysis. Pergamon, 18(1), pp. 12–24. Shu, J. Y., King, W. E. and Fleck, N. A. (1999) 'Finite elements for materials with strain gradient effects', International Journal for Numerical Methods in Engineering, 44(3), pp. 373–391.

Sluis, O. van der et al. (1999) 'Homogenization of heterogeneous polymers', International Journal of Solids and Structures, 36(21), pp. 3193–3214.

Stroeven, M., Askes, H. and Sluys, L. J. (2004) 'Numerical determination of representative volumes for granular materials', Computer Methods in Applied Mechanics and Engineering, 193(30–32), pp. 3221–3238.

Suquet, P. M. (1985) 'Local and global aspects in the mathematical theory of plasticity', Plasticity today: modelling, methods and applications, pp. 279–310.

Šamec, B., Potrč, I. and Šraml, M. (2011) 'Low cycle fatigue of nodular cast iron used for railway brake discs', Engineering Failure Analysis. Pergamon, 18(6), pp. 1424–1434.

Toupin, R. A. (1964) 'Theories of elasticity with couple-stress', Archive for Rational Mechanics and Analysis. Springer-Verlag, 17(2), pp. 85–112.

Xue, H. Q., Bayraktar, E. and Bathias, C. (2008) 'Damage mechanism of a nodular cast iron under the very high cycle fatigue regime', Journal of Materials Processing Technology. Elsevier, 202(1–3), pp. 216–223.

Zervos, A., Papanicolopulos, S. and Vardoulakis, I. (2009) 'Two Finite-Element Discretizations for Gradient Elasticity', Journal of engineering mechanics, 135(3), pp. 203–213.

Zhu, H. T., Zbib, H. M. and Aifantis, E. C. (1997) 'Strain gradients and continuum modeling of size effect in metal matrix composites', Acta Mechanica. Springer-Verlag, 121(1–4), pp. 165–176.